energies

MDPI

Article

Validating Meteosat Second Generation and Himawari-8 Derived Solar Irradiance against Ground Measurements: Solarad AI's Approach

Jitendra Kumar Meher [1], Syed Haider Abbas Rizvi [1,2,*], Bhramar Choudhary [1], Ravi Choudhary [1], Yash Thakre [1], Ritesh Kumar [1] and Vikram Singh [2]

[1] Solarad AI, Building 145, 91 Springboard, Sector-44, Gurugram 122003, Haryana, India; jitendra.meher@solarad.ai (J.K.M.); bhramar@solarad.ai (B.C.); ravi@solarad.ai (R.C.); yash.thakre@solarad.ai (Y.T.); ritesh.kumar@solarad.ai (R.K.)

[2] Department of Chemical Engineering, Indian Institute of Technology Delhi, Hauz Khas, New Delhi 110016, India; vs225@iitd.ac.in

* Correspondence: haider@solarad.ai

Abstract: This study assesses the efficacy of the Heliosat-2 algorithm for estimating solar radiation, comparing its outputs against ground measurements across seven distinct countries: the Netherlands, Spain, Japan, Namibia, South Africa, Saudi Arabia, and India. To achieve this, the study utilizes two distinct satellite data sources—Himawari-8 for Japan and Metosat Second Generation-MSG for the rest of the countries—and spanning the time between January 2022 and April 2024. A robust methodology for determining albedo parameters specific to Heliosat-2 was developed. During cloudy days, the estimates provided by Heliosat-2 generally exceeded the ground measurements in all of the countries. Conversely, on clear days, there was a tendency for underestimation, as indicated by the median values of the mean bias (MB) across most of the countries. The Heliosat-2 model slightly underestimates daily radiation values, with a median MB ranging from −27.5 to +10.2 $W \cdot m^{-2}$. Notably, the median root mean square error (RMSE) on clear days is significantly lower, with values ranging from 24.8 to 108.7 $W \cdot m^{-2}$, compared to cloudy days, for which RMSE values lie between 75.3 and 180.2 $W \cdot m^{-2}$. In terms of R^2 values, both satellites show strong correlations between the estimated and actual values, with a median value consistently above 0.86 on a monthly scale and over 92% of daily data points falling within ±2 standard deviations.

Keywords: BSRN; Heliosat-2; Himawari-8; Meteosat-MSG; renewable energy; solar radiation; validation study

check for updates

Citation: Meher, J.K.; Rizvi, S.H.A.; Choudhary, B.; Choudhary, R.; Thakre, Y.; Kumar, R.; Singh, V. Validating Meteosat Second Generation and Himawari-8 Derived Solar Irradiance against Ground Measurements: Solarad AI's Approach. *Energies* **2024**, *17*, 2913. https://doi.org/10.3390/en17122913

Academic Editors: Fabio Montagnaro and Roberto Solimene

Received: 15 May 2024
Revised: 5 June 2024
Accepted: 10 June 2024
Published: 13 June 2024

Copyright: © 2024 by the authors. Licensee MDPI, Basel, Switzerland. This article is an open access article distributed under the terms and conditions of the Creative Commons Attribution (CC BY) license (https://creativecommons.org/licenses/by/4.0/).

1. Introduction

Measuring solar radiation is crucial for various applications, including climate monitoring and weather forecasting, and is particularly important for the development and optimization of renewable energy projects. Accurate solar radiation data are essential for optimizing solar energy applications and validating models that forecast long-term daily global radiation levels, aiding in the efficient deployment and management of solar energy systems [1,2]. Furthermore, accurate solar radiation data are indispensable for environmental and climate studies, impacting sustainable energy solutions aimed at mitigating climate change [3]. The importance of disseminating best practices in solar radiation measurement and modelling is emphasized, highlighting their significance in educational and operational contexts within the solar industry [4]. These efforts collectively facilitate the efficient deployment of solar technologies, enhancing energy management systems and contributing to sustainable-development goals.

Solar radiation data are derived from various sources, including ground-based measurements, satellite observations, and reanalysis datasets, each offering unique insights

into solar energy patterns and dynamics. Ground-based measurements, such as those obtained from pyranometers, pyrheliometers, and weather stations, provide direct and accurate assessments of solar radiation at specific locations. For example, the World Radiation Monitoring Center–Baseline Surface Radiation Network (WRMC-BSRN) operates globally distributed ground stations equipped with high-quality instruments to measure solar radiation parameters [5]. These measurements contribute data valuable for understanding regional variations in solar radiation and their impacts on climate and energy systems. Within the realm of climate change research, BSRN data have been instrumental in investigating global phenomena, such as solar dimming and brightening [6,7]. In the context of energy systems, these data have been crucial in validating the frequency and ramp distributions pertinent to studies focusing on low-voltage grid dynamics [8]. Satellite observations complement ground measurements by providing global coverage and continuous monitoring. Satellites like Himawari, Meteosat Second Generation (MSG), GOES (Geostationary Operational Environmental Satellites), and INSAT (Indian National Satellite System) offer geostationary perspectives, capturing solar radiation data over specific regions with a high temporal resolution [9]. These satellites are instrumental in weather forecasting, solar energy planning, and monitoring meteorological phenomena. Reanalysis datasets, such as ECMWF-ERA5 (European Centre for Medium-Range Weather Forecasts–Fifth Generation Reanalysis) and MERRA2 (Modern-Era Retrospective Analysis for Research and Applications, version 2), merge observations with numerical models to offer consistent and gridded records of solar radiation and other meteorological parameters over time and space [10]. These datasets are invaluable for climate studies, renewable energy planning, and the understanding of historical solar radiation patterns.

Satellite data estimate the solar radiation on Earth's surface via remote sensing [11]. While they offer broad coverage and frequent updates, ground-based data sources provide precise measurements, but are limited to specific locations. Reanalysis data merge observations with models based on historical records, but may have biases and uncertainties [12]. Integrating these datasets requires validation, the addressing of uncertainties, and the combination of sources for reliable solar radiation estimates.

Various methods are utilized to extract solar irradiance from satellite data, including empirical models that rely on historical data, physical models based on principles of physics, statistical methods used for analyzing data patterns, machine learning approaches trained on satellite–ground measurements, and radiative transfer (RT) models simulating the solar radiation's interaction with the atmosphere [13]. Each method offers unique advantages and limitations, catering to differences in data availability, computational resources, and accuracy requirements. Among the methods employed for extracting solar irradiance from satellite data, the Heliosat method [14,15] stands out for its unique approach to approximating cloud transmission, one based on satellite-observed digital counts or calibrated radiance values. This method is particularly useful in converting satellite cloud index data to solar irradiance values, which is essential for solar radiation forecasting and energy applications. Case studies in which the Heliosat method has been used include short-term forecasting of solar radiation [11,16,17], solar energy assessment using remote sensing technologies [18,19], and the deriving of shortwave solar radiation from satellite images [11,20]. The advantages of the Heliosat method include its ability to derive cloud transmission values from satellite data, its adaptability to different satellite sensors, and its capability to provide estimates of solar irradiance based on cloud cover information, contributing to improved solar energy forecasting and resource assessment.

The accuracy of solar irradiance data derived from the Meteosat Second Generation Spinning Enhanced Visible and Infrared Imager (SEVIRI) satellite operating over countries in the European Union (EU), particularly southern Spain and Switzerland, was assessed for the year 2015 using a Heliosat-based method called HelioMont, with reference to in situ measurements [21]. The results indicate that under all-sky conditions, the mean biases (MB) varied from approximately -5.0 W·m^{-2} to 55.0 W·m^{-2}. The root mean square error (RMSE) ranged approximately between 175.0 W·m^{-2} and 195.0 W·m^{-2}. The validation

approach employed revealed correlation coefficients (specifically Pearson's correlation coefficient, r) for HelioMont and the in situ data within a range of 0.79 to 0.92. This indicates a robust correlation between the satellite-derived solar irradiance data and the ground-based measurements.

For parts of the Indian subcontinent in the South Asian region, the utilization of the Heliosat method indicates a generally positive bias in the estimated daily Global Horizontal Irradiance (GHI), as compared to ground measurements, from 2000 to 2007, typically within a range of 5%, with an RMSE averaging around 12.0% [22]. Conversely, another study [23] conducted in the Indian subcontinent employed a remote sensing-based method known as the Indian Solar Irradiance Operational System (INSIOS) to assess ground GHI measurements for the year 2018. The GHI output determined through this method during clear-sky conditions predominantly resulted in underestimations when compared to ground measurements. The MB (and RMSE) ranged from −12.5 (and −19.7) to −143.3 (206.5) $W \cdot m^{-2}$ across different seasons. Similarly, during cloudy conditions, the model tended to overestimate ground observations. The MB (and RMSE) varied from −35.7 (47.4) to 389.6 (427.3) $W \cdot m^{-2}$.

Meanwhile, for parts of the Middle East region, the Heliosat method, when used for the time range of 2011–2014, yielded predominantly negative biases for the hourly data, with results ranging from −7.0% to 4.0% for all-sky conditions, and from −8.0% to 3.0% for clear-sky conditions. Under cloudy-sky conditions, biases vary significantly between stations, ranging from 16.0% to 85.0%. The relative root mean square error (%RMSE) ranges between 12.0% to 20.0% for all-sky conditions and 8.0% to 12.0% for clear-sky conditions, but notably increases to above 56.0% under cloudy-sky conditions [24].

As for parts of the African region, a study [25] was conducted to evaluate the performance of the Heliosat-based validation method against hourly ground GHI across four typical climatic zones, using entire-year data from 2015. The study reported %RMSE values ranging from 10.4% to 12.7%, with nominal MB values falling between −0.97% and 0.39%.

Considering parts of the East Asian region, the Heliosat-based estimation of GHI against observed data for the time range of 2011–2013 indicated overall relative mean bias deviations (%MB) and %RMSE in daily solar irradiance retrieval values of about 5.0 and 15.0%, respectively. Seasonally, the largest %MB and %RMSE of retrieved daily solar irradiance occurred in spring (9.5 and 21.3%, on average), while the lowest %MB (−0.3%, on average) and %RMSE (9.7%, on average) occurred in autumn and winter, respectively [26].

Validation studies addressing the Heliosat method play a crucial role in evaluating its accuracy in estimating solar irradiance, ensuring the reliability of its outputs, and pinpointing areas for algorithm enhancement [27]. The present study endeavors to bridge several research gaps within the field.

- Firstly, while prior validation studies of the BSRN predominantly utilized data predating 2022, our investigation focuses on a more recent timeframe, utilizing data spanning from 2022 to 2024. This temporal shift ensures that our analyses remain relevant and reflective of current conditions, including the potential impacts of climate change on solar radiation patterns.
- Secondly, unlike previous studies that relied solely on either Himawari-8 or MSG datasets for validation, this study utilizes both datasets to cover a broader range of observational locations. Himawari-8 data will be used for the East Asia region, while MSG data will cover the EU, Africa, the Middle East, and South Asia. This approach leverages dedicated satellites for each respective region to derive irradiance, using the same algorithm, and with spatial re-gridding. The datasets generated from 2023 and 2024 will present current trends in solar radiation across these regions.
- Lastly, a key objective of our study is the application and refinement of existing methodologies for determining albedo parameters specific to Heliosat-2. We aim to achieve significant improvements in the accuracy and reliability of modeled solar radiation datasets, and therefore, the exactness of the input parameters is crucial.

In Section 2, the study addresses the examination of study sites, the utilization of various satellite and ground data, and the methodology employed for extracting GHI data from satellite images, alongside the validation process, which uses different indices against ground datasets. Section 3 presents the obtained results, emphasizing the comparison between satellite and ground data across different sky conditions and assessing the performance of the two satellites in capturing seasonal GHI values. Section 4 further discusses these findings, contextualizing them within previous research endeavors and elucidating any agreements or discrepancies encountered. Finally, Section 5 succinctly encapsulates the key conclusions drawn from the study's findings.

2. Materials and Methods

2.1. Study Area and Datasets Used

In this study, data were collected from various solar monitoring stations located across several different countries, including Cabauw, in the Netherlands; Cener, in Spain; Abashiri and Tateno, in Japan; Gobabeb, in Namibia; USAid Venda, in South Africa; and Saudi West Coast, in Saudi Arabia. Ground data were sourced from different networks, such as the World Radiation Monitoring Center–Baseline Surface Radiation Network (BSRN—https://bsrn.awi.de/, accessed on 19 April 2024) [5] and the Southern African Universities Radiometric Network (SAURAN—https://sauran.ac.za/, accessed on 19 April 2024) [28] (https://dataportals.pangaea.de/bsrn/stations, accessed on 19 April 2024), while some stations utilized SCADA (Supervisory Control and Data Acquisition) systems for ground data collection. The details of metadata of the locations used in the present study have been given in Table 1.

Table 1. Metadata of locations used. The Analysis Period column shows the time period for which the statistical analysis was performed. For locations in the Middle East and South Asia, the ground data was taken from the SCADA site.

Station Name	Short Names	Lat (° N/S)	Lon (° E/W)	Country (Region)	Ground Data Source	Satellite Data Source	Analysis Period	Reference
Cabauw	CAB	51.96	4.92	Netherlands (European Union)	BSRN	MSG-1 and -2	January 2022–February 2024	[29]
Cener	CNR	42.81	−1.60	Spain (European Union)	BSRN	MSG-1 and -2	January 2022–January 2024	[30]
Abashiri	ABS	44.01	144.27	Japan (East Asia)	BSRN	Himawari-8	January 2023–October 2023	[31]
Tateno	TAT	36.05	140.12	Japan (East Asia)	BSRN	Himawari-8	January 2023–February 2024	[32]
Gobabeb	GOB	−23.56	15.04	Namibia (Africa)	BSRN	MSG-1 and -2	January 2022–December 2023	[33]
USAid Venda	VUW	−23.13	30.42	South Africa (Africa)	SAURON	MSG-1 and -2	January 2022–December 2023	[28]
Saudi West Coast	KSA	22.58	39.16	Saudi Arabia (Middle East)	Ground SCADA	MSG-1 and -2	August 2023–January 2024 March 2024–April 2024	-
Ashok Nagar	ASO	24.52	77.62	India (South Asia)	Ground SCADA	MSG-1 and -2	January 2023–October 2023	-
Honnali	HON	14.20	75.56	India (South Asia)	Ground SCADA	MSG-1 and -2	January 2023–October 2023	-

The global positioning of the locations can be determined using Figure 1. Quality controls undertaken for the SAURAN data can be assessed from [28]. Similarly, quality control information for the BSRN data is available in [5]. Additionally, all irradiance data collected for this study undergo a quality control routine, as described by [34], whereby irradiance data points are tested as to their physical acceptability and extreme limits. We also remove any time step with zenith angles above 85° due to the questionable accuracy of measured data at these times.

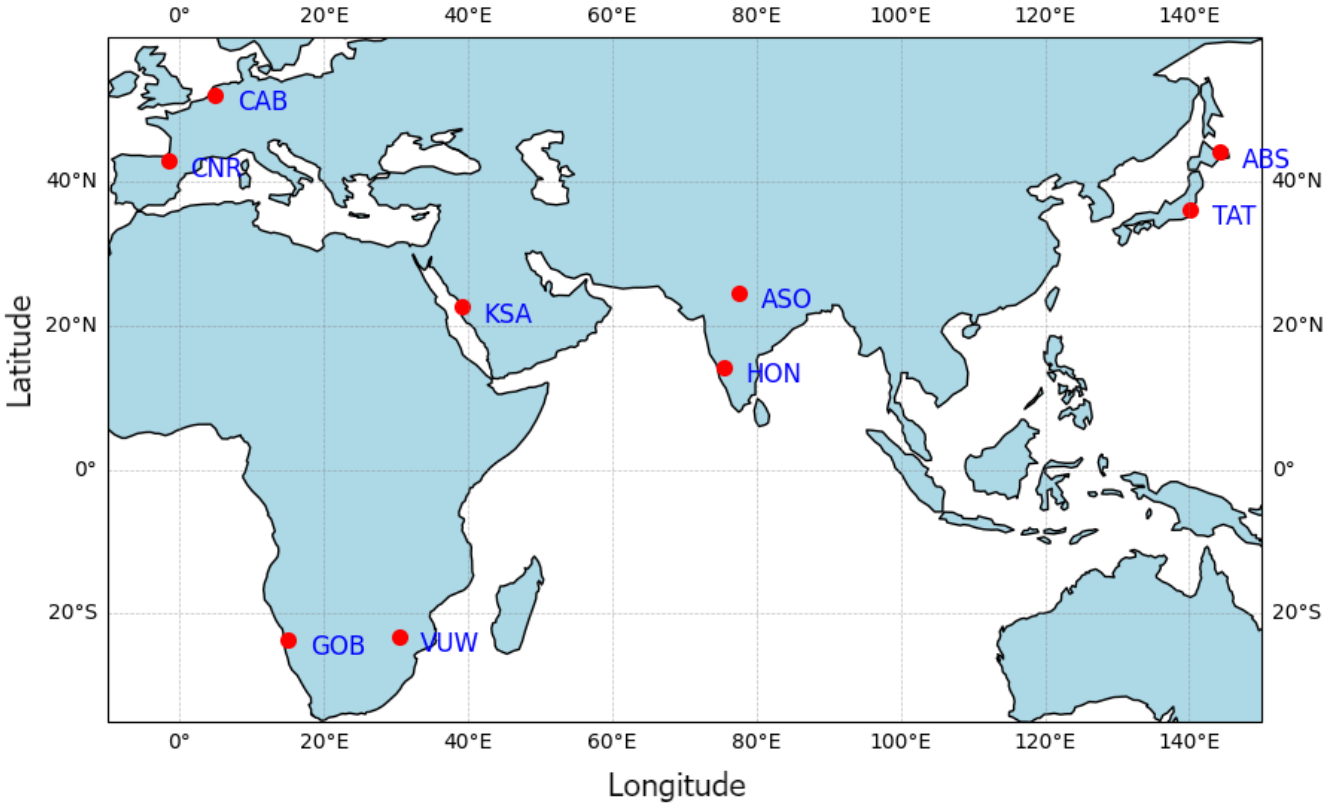


Figure 1. Global positioning of the locations used in this study. The locations' labels are the short names of the sites, adopted from Table 1.

The choice of satellite data sources for these stations depended on the availability and coverage of satellite scans over the respective regions. In the cases of locations in Japan, such as Abashiri (ABS) and Tateno (TAT), the Himawari-8 satellite system was utilized due to its comprehensive coverage and high-resolution imagery, which is specifically tailored for East Asian regions. Conversely, for stations in other countries like the Netherlands, Spain, Namibia, South Africa, Saudi Arabia, and India, the MSG satellite system was employed, as its coverage extends to a broader geographical area outside of East Asia.

We leveraged images from the 0.64 micrometer (μm) band in the visible (red) channel of the "Advanced Himawari Imager (AHI)" on the Himawari-8 geostationary satellite, operated by the Japan Meteorological Agency (JMA), accessible at https://himawari8.nict.go.jp/, accessed on 19 April 2024. The VIS0.64 channel of the Himawari-8 AHI measures data in the spectral band ranging from 0.555 to 0.721 μm, with a central wavelength of 0.6399; it is accessible at https://www.data.jma.go.jp/mscweb/en/himawari89/space_segment/spsg_ahi.html, accessed on 19 April 2024. The full-disk images from Himawari-8 used in this study spanned from 60° N to 60° S in latitude and from 80° E to 160° W in longitude. These images, updated every 10 min, had a spatial resolution of 5 km and can be accessed at https://www.eorc.jaxa.jp/ptree/userguide.html, accessed on 19 April 2024.

Furthermore, we integrated Indian Ocean Data Coverage (IODC) imagery from the visible 0.6 μm channel of the "High Rate Spinning Enhanced Visible Infra-Red Imager

(SEVIRI)" on the MSG satellite, operated by the European Organisation for the Exploitation of Meteorological Satellites (EUMETSAT); the data are available at (https://view.meteosat.int/, accessed on 19 April 2024). Images captured before June 2022 were sourced from MSG-1 (Meteosat-8), while those from June 2022 onward were obtained from MSG-2 (Meteosat-9), following the conclusion of the MSG-1 mission on 1 July 2022. The VIS0.6 channel of MSG SEVIRI belongs to the visible and near-infrared spectrum and has a central wavelength of 0.635 µm and a spectral band ranging from 0.56 to 0.71 µm [35]. In this study, the full-disk images from the MSG satellite covered a range from 77° N to 77° S in latitude and from 31° W to 122° E in longitude. The images were updated every 15 min, with a spatial resolution of 3 km; the data are accessible at https://view.eumetsat.int/productviewer/productDetails/msg_iodc:vis006?v=default, accessed on 19 April 2024.

2.2. Methodology

This section delineates the Heliosat-2 algorithm, an advanced methodology for estimating solar irradiance from satellite imagery and ground observations. The approach integrates sophisticated image classification techniques, using deep learning, rigorous statistical analyses, and empirical calculations to ensure precision in solar irradiance values. Additionally, the validation of this method employs robust statistical indices which quantify the accuracy of the Heliosat-2 estimates in comparison to ground-based measurements. Due to the different spatial resolutions of the Himawari-8 and MSG images, the Himawari-8 images were first re-gridded to match the resolution of MSG (i.e., 3 km) before the implementation of Heliosat-2 method. Spatial re-gridding helps reduce systematic bias due to resolution mismatch and is a common practice which has been followed in several studies [36–38].

2.2.1. Heliosat-2

Below is a detailed explanation of the methodology and implementation of the Heliosat-2 algorithm for estimating solar irradiance, presenting a systematic approach to analyzing satellite imagery and ground observations to derive accurate solar irradiance values. Figure 2 shows the flowchart of the Heliosat-2 algorithm followed in this study.

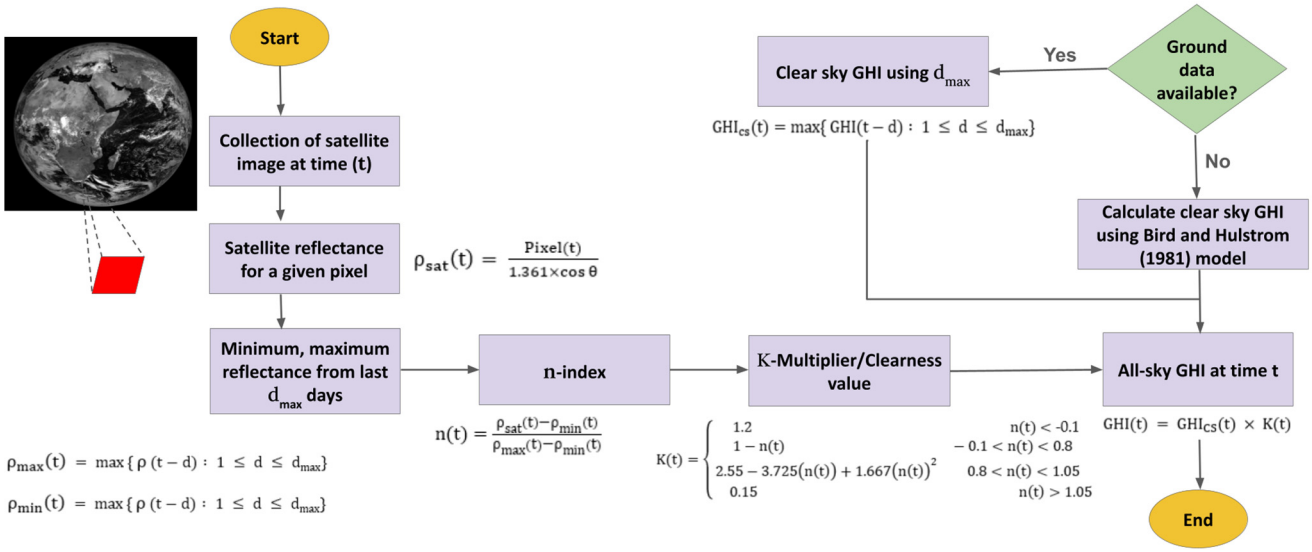


Figure 2. Flowchart showing the algorithms used for the all-sky GHI estimation using Heliosat-2.

- Step 1: Generate Clear-Sky Global Horizontal Irradiance (GHI_{cs}).

Here, the method utilizes the most recent ground GHI observations from the past to generate the clear-sky GHI for a specific timestamp (t):

$$GHI_{cs}(t) = \max\{GHI(t-d) : 1 \leq d \leq d_{max}\} \quad (1)$$

where, d_{max} is the number of days considered in the calculation of clear-sky conditions.

Alternatively, a Bird clear-sky model [39] can be used to calculate $GHI_{cs}(t)$, depending on the availability of on-site clear-sky solar radiation dataset to estimate the coefficients in a solar radiation model [40]. A Bird clear-sky model takes into account factors such as the position of the sun, solar zenith angle, atmospheric conditions (such as water vapor and aerosols), and surface albedo (reflectivity).

- Step 2: Calculate Satellite Reflectance Value.

Determine the satellite reflectance value for the given timestamp (t) by analyzing the pixel value of the satellite image.

$$\rho_{sat}(t) = \frac{Pixel(t)}{1.361 \times \cos\theta} \quad (2)$$

Here, $\rho_{sat}(t)$ is the reflectance of the satellite, $Pixel(t)$ represents the pixel value, and the solar constant is taken as 1.361 $kW \cdot m^{-2}$, while θ is the solar zenith angle.

- Step 3: Calculate Minimum and Maximum Satellite Reflectance Values.

$$\rho_{max}(t) = \max\{\rho(t-d) : 1 \leq d \leq d_{max}\} \quad (3)$$

$$\rho_{min}(t) = \max\{\rho(t-d) : 1 \leq d \leq d_{max}\} \quad (4)$$

This helps in establishing the minimum and maximum satellite reflectance values to delineate the range of potential cloud cover.

In determining the albedo parameters, we take cues from both Bechet et al. [27] and Cros et al. [41].

The models developed by Bechet et al. and Cros et al. both represent significant advancements in the field of solar irradiance estimation, though they focus on different aspects of the issue. The model involved in Bechet et al. is primarily concerned with quantifying cloud cover through a cloudiness index labeled 'n', which is integral to understanding and predicting the solar irradiation that reaches the Earth's surface within a given area. The model operates on the principle that cloud cover significantly influences solar irradiance; by assessing the clarity of the sky through digital counts, it estimates the GHI. This methodology provides a focused approach for dealing with variability in cloud cover and determining its direct impact on solar energy reception. Conversely, the method in Cros et al. broadens the scope by not only addressing cloud cover but also integrating a comprehensive analysis of other atmospheric conditions, including aerosols, ozone, and water vapor, through RT modeling. Their technique retrieves a long time-series of spectrally resolved all-sky radiance, enhancing the accuracy of irradiance data under both clear and cloudy-sky conditions.

For $\rho_{max}(t)$, representing the maximum reflectance from cloudy pixels, we follow Cros et al.'s approach of selecting the 95th percentile of reflectance values at local noon, ensuring robustness against outliers and changes in sensors. Local noon is when the sun is highest in the sky, marking its maximum altitude angle, which is known as the solar zenith angle. This varies based on location and time of year due to factors like Earth's tilt and orbit. This is why the solar zenith angle is always at its minimum during local noon, making it distinct from the surrounding times. As for $\rho_{min}(t)$, denoting ground albedo from a clear-sky pixel, we blend methods, leaning towards the rationale described in the study of Bechet et al. We opt for the second minimum albedo within a d_{max} time frame to mitigate potential image defects, ensuring reliability. The d_{max} was fixed to a rolling window of 60 days in the current study.

- Step 4: Calculate Cloudiness Index (*n*-index).

This step computes the cloudiness index, or *n*-index, or $n(t)$, for which a higher value indicates a greater presence of clouds in the observed area.

$$n(t) = \frac{\rho_{sat}(t) - \rho_{min}(t)}{\rho_{max}(t) - \rho_{min}(t)} \quad (5)$$

- Step 5. Calculate K-Multiplier or Clearness Value.

Here the K-multiplier, representing the clearness of the sky, and based on the calculated cloudiness index, is filtered out from an empirical set of values, as given below.

$$K(t) = \begin{cases} 1.2 & n(t) < -0.1 \\ 1 - n(t) & -0.1 < n(t) < 0.8 \\ 2.55 - 3.725(n(t)) + 1.667(n(t))^2 & 0.8 < n(t) < 1.05 \\ 0.15 & n(t) > 1.05 \end{cases} \quad (6)$$

- Step 6. Calculate GHI.

This step utilizes the previously determined clear-sky GHI, along with the K-multiplier, to calculate the GHI for the given timestamp (t).

$$GHI(t) = GHI_{CS}(t) \times K(t) \quad (7)$$

2.2.2. Comparison Metrics

Three statistical indices were used to quantify degree of agreement/disagreement between the GHI estimates of Heliosat-2 ($\hat{y}_i$) and ground measurements (y_i): the coefficient of determination (R^2), mean bias (MB), and root mean square error (RMSE); these equations are given below.

$$R^2 = 1 - \frac{\sum_{i=1}^{n} (y_i - \hat{y}_i)^2}{\sum_{i=1}^{n} (y_i - \overline{y})^2} \quad (8)$$

where, $\overline{y}$ represents the mean of the ground measurements.

$$MB = \frac{1}{n}\sum_{i=1}^{n}(\hat{y}_i - y_i) \quad (9)$$

$$RMSE = \sqrt{\frac{1}{n}\sum_{i=1}^{n}(y_i - \hat{y}_i)^2} \quad (10)$$

R^2 quantifies the proportion of variability in the ground GHI measurement that is explained by the Heliosat-2 estimates, facilitating model evaluation regardless of scale. MB assesses the average error between Heliosat-2 and ground GHI values, providing insight into overall prediction accuracy. In contrast, RMSE encapsulates the average magnitude of the differences between Heliosat-2 and ground GHI values, with lower values indicating better model performance. RMSE's sensitivity to large errors, interpretability in the units of the predicted variable, and robustness to outliers render it a versatile and informative metric for assessing predictive model accuracy.

2.2.3. Distinction between Clear and Cloudy Days

To distinguish between clear-day and cloudy-day conditions, we utilized the popular clearness index. The clearness index is the ratio of the mean measured GHI (here, ground data) to the mean top-of-atmosphere irradiance (extraterrestrial irradiance) [42–44]. The extraterrestrial irradiance was calculated using the 'get_extra_radiation' function from the PVLIB v0.10.4 Python package [45,46], which accounts for factors such as the solar zenith angle, Sun–Earth distance, day length, and solar constant. The 'clearness_index' function

of PVLIB v0.10.4 was then used to compute the clearness index, based on the previously calculated extraterrestrial irradiance, measured GHI, and solar zenith angle.

Days with a mean clearness index value below 0.7 were classified as cloudy, while those with values above 0.7 were considered clear, following the standard procedures defined in [42,43].

3. Results

We conducted a thorough comparison between the solar radiation estimates generated by the Heliosat-2 model and ground measurements across diverse geographic locations: the Middle East, East Asia, and Africa. This analysis encompassed various categories, including hourly comparison, diurnal comparison (includes both clear-sky and cloudy-sky conditions), monthly comparison, and seasonal comparison.

3.1. Validation of Mean Diurnal Radiation

Figure 3 illustrates the range of R^2 values, spanning from 0.54 to 0.99, across all locations. Specifically, the R^2 values for both EU locations were markedly different from each other. While the Cabauw (CAB) location demonstrated a fairly good agreement between satellite-derived and ground-based GHI estimates, with an R^2 value of 0.81 (Figure 3A), the Cener (CNR) location exhibited a poor comparison result, with an R^2 value of 0.51 (Figure 3B). The R^2 value for Japanese sites employing Himawari-8 images [Abashiri (ABS) and Tateno (TAT)] stands at 0.91, as indicated in Figure 3C,D. Conversely, Heliosat-2 estimates of GHI from MSG images exhibit a mean R^2 value of 0.95 for African locales [Gobabeb (GOB) and USAid Venda (VUW)], as depicted in Figure 3E,F. Notably, the Saudi West Coast (KSA) location in Saudi Arabia boasts the highest R^2 value, of 0.99, as evidenced in Figure 3G. The R^2 values for the Ashok Nagar (ASO) and Honnali (HON) locations in India were identical and show a fairly good correlation (0.86) between the model and the ground GHI, as evident in Figure 3H,I respectively. Across all locations, more than 92.4% of data points fell within a range of ± 2 standard deviations (SD).

Regarding predicted GHI estimates, two EU locations show an overestimation in terms of MB, ranging from +9.7 to +20.60 $W \cdot m^{-2}$ (Figure 3A,B). Similarly, overestimations were also found for the two Japanese locations, with MB ranging from ~3.0 to 11.9 $W \cdot m^{-2}$ (Figure 3C,D). Conversely, African sites in GOB and the Saudi Arabian location of KSA exhibit underestimations ranging from -5.6 to~-29.0 $W \cdot m^{-2}$. RMSE values range from a minimum of 13.8 $W \cdot m^{-2}$ in the KSA location to a maximum of approximately 46.0 $W \cdot m^{-2}$ in GOB. In India, the satellite GHI estimates show a minor overestimation of +7.5 $W \cdot m^{-2}$, while a nominal underestimation was observed in HON, with an MB of -2.3 $W \cdot m^{-2}$. The RMSE values across all the locations varies from a minimum of 13.8 $W \cdot m^{-2}$ in KSA to a maximum of 71.2 in CNR.

3.2. Validation of Diurnal Radiation

Figure 4A displays the R^2 values depicting the correlation between the diurnal estimates of Heliosat-2 GHI and ground data. Meanwhile, Figure 4B,C exhibit the MB and RMSE, respectively. In Figure 4A, the median R^2 values exhibit an inclining trend as we transition from CAB to KSA locations and a declining nature from KSA to HON, with most values surpassing 0.8, excepting CAB and CNR. The interquartile range (IQR) for the KSA is the narrowest, followed by GOB and VUW, while it is widest for CAB, followed by CNR. The widest ranges of IQR, in the two locations of CAB and CNR, show that for at least 25% of days, the estimated GHI and ground measurements had R^2 values of less than 0.65 and 0.75, respectively.

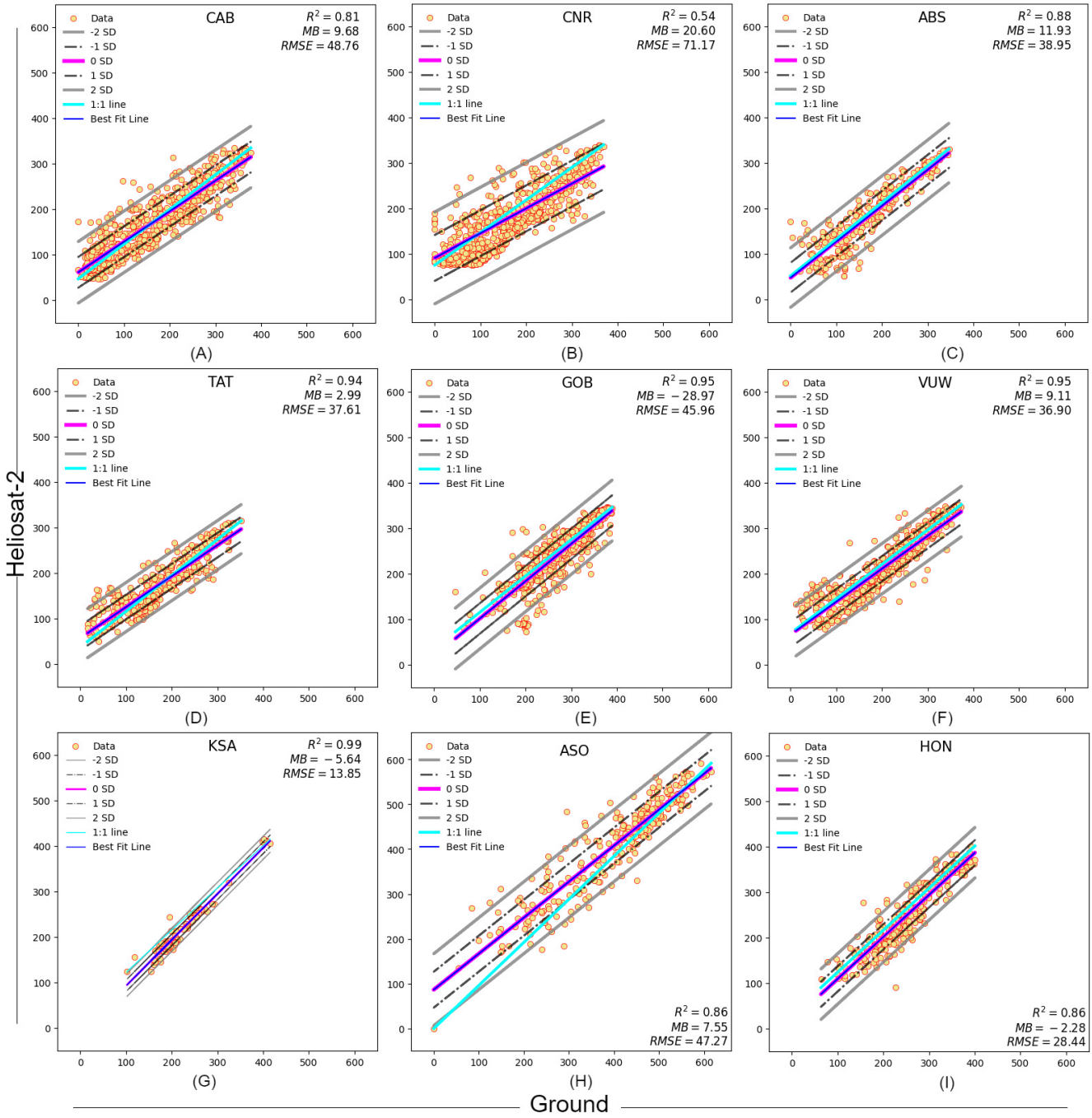


Figure 3. Comparisons of mean diurnal ground and Heliosat-2 GHI estimates in terms of scatter plots for (**A**) CAB, (**B**) CNR, (**C**) ABS, (**D**) TAT, (**E**) GOB, (**F**) VUW, (**G**) KSA, (**H**) ASO, and (**I**) HON sites, irrespective of clear and cloudy days. The 1:1 line indicates where ground and Heliosat-2 data are identical. The zero standard deviation line (magenta) overlaps with the best-fit line. The negative standard deviation lines lie below the best-fit line, while the positive standard deviation lines lie above it.

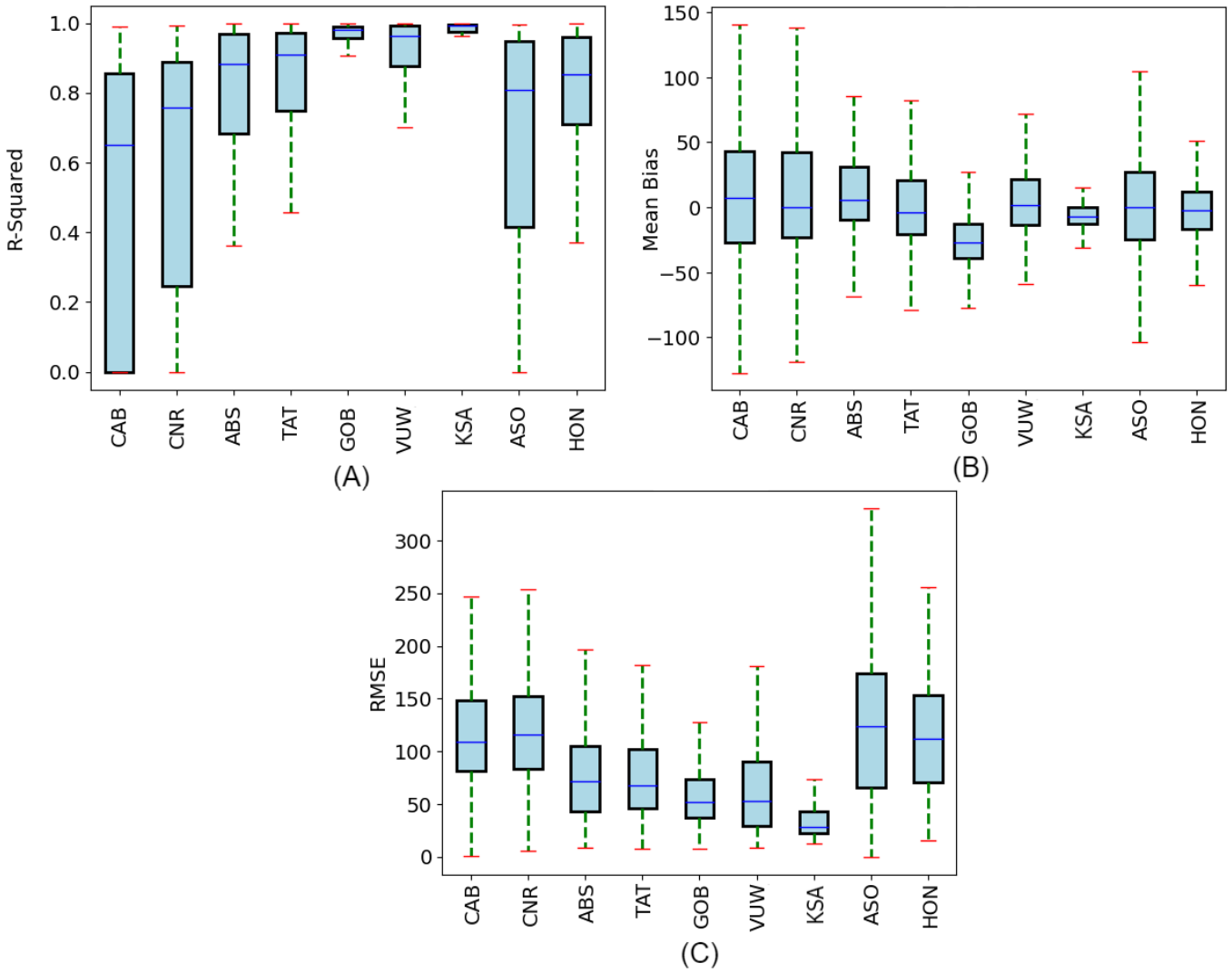


Figure 4. Comparisons of ground and Heliosat-2 GHI estimates in terms of (**A**) R^2, (**B**) MB (in $W{\cdot}m^{-2}$), and (**C**) RMSE (in $W{\cdot}m^{-2}$) values for the diurnal radiation, irrespective of clear and cloudy days.

The MB fluctuates significantly across the dataset, ranging from −130.7 to +145.2 $W{\cdot}m^{-2}$ (Figure 4B). Analyzing the median MB, Heliosat-2′s estimates show a nominal bias in CAB and CNR, lying close to zero, while they have the highest range and IQR among all of the locations in this study. A slight underestimation of daily radiation values, averaging −5.1 $W{\cdot}m^{-2}$, was observed in TAT. Conversely, in ABS, there is an average overestimation of approximately +5.2 $W{\cdot}m^{-2}$. Assessing the MB across the African sites, Heliosat-2′s estimates portray a tendency towards underestimation (−29.8 $W{\cdot}m^{-2}$) for the majority of daily radiation values in GOB, while in VUW, a minor overestimation (+3.4 $W{\cdot}m^{-2}$) is observed, based on median values of MB throughout the study period (Figure 4B). The MB analysis in the KSA location of Saudi Arabia indicates that Heliosat-2 estimates slightly underestimate daily radiation values (clear + cloudy days) by a median value of approximately −10.5 $W{\cdot}m^{-2}$. Both of the Indian locations show a nominal median MB, close to zero. The HON location shows less uncertainty in terms of lower MB IQR and MB range across the study period for India.

Moreover, the RMSE data for Japan, depicted in Figure 4C, suggests relatively higher variability compared to the Middle East, with daily values ranging from 5.2 $W{\cdot}m^{-2}$ to 195.0 $W{\cdot}m^{-2}$ and an average median value of 71.9 $W{\cdot}m^{-2}$, irrespective of sky conditions. Similarly, the analysis of RMSE data for the African region, as shown in Figure 4C, indicates a range of RMSE values between 9.6 $W{\cdot}m^{-2}$ and 185.0 $W{\cdot}m^{-2}$, with an average median

value of 52.7 W·m^{-2} on a daily time scale (inclusive of clear and cloudy days). The ASO location in India has the highest variability of RMSE values, ranging from 0 to nearly 341.7 W·m^{-2}.

3.2.1. Validation under a Daily Clear-Sky Condition

On days classified as clear (as shown in Figure 5A), the median R^2 consistently exceeds 0.90 in all the regions except for the locations in the EU (median $R^2 > 0.75$), with African locations consistently surpassing 0.97. Under such conditions, the average median MB values for both EU locations were nearly zero (though they have the highest variability among all the locations) while the average of the median MB for both Japanese locations was −3.5 W·m^{-2}, ranging from −77.3 to +50.6 W·m^{-2} (Figure 5B). Similarly, the median MB indicates an overall underestimation for both African locations, at −27.7 W·m^{-2} in GOB and +7.6 W·m^{-2} in VUW. In the KSA location, the median value of the MB is −7.2 W·m^{-2}, with a range from −10.1 to −0.5 W·m^{-2} for the 25th to 75th percentiles of clear days' data. In India, the MB in clear days varies from −77.3 to 73.8 W·m^{-2}.

The highest RMSE for clear sky was observed in the CNR location, with a median value of 108.6 W·m^{-2}. In contrast, clear days presented lower RMSE values for both Japanese locations, averaging a median of 52.5 W·m^{-2} (Figure 5C). In African locations, particularly on clear days, the median RMSE value hovers around 41.6 W·m^{-2}, with both GOB and VUW exhibiting similar error bars, ranging from approximately 7 to 115 W·m^{-2}. In the KSA site, the RMSE values were notably lower, ranging from 16.2 W·m^{-2} to 58.7 W·m^{-2} (Figure 5C). The Indian locations showed the highest variability of RMSE values (0 to 250 W·m^{-2}) under clear-sky conditions among all the locations analyzed in this study.

3.2.2. Validation under Daily Cloudy-Sky Conditions

In overcast conditions, the median values of R^2 across all the locations remained at less than 0.85. The ASO location in India shows the lowest median R^2 value, of approximately 0.23 (followed by 0.43 for CAB in the EU region), while it was highest for VUW. Under cloudy conditions, among the Japanese sites, R^2 values drop to approximately 0.61 for TAT and 0.71 for ABS, as illustrated in Figure 5D. In contrast, the African region shows a less pronounced reduction under similar conditions, with median R^2 values falling to about 0.72 for GOB and 0.88 for VUW, from a baseline of near-perfect correlation ($R^2 = 0.98$) on clear days. Similarly, in the KSA location, the decrease in R^2 value seen on cloudy days is to approximately 0.88, underscoring a universal trend of diminished solar radiation, which is predictable during overcast weather.

Furthermore, the MB in solar radiation estimates under cloudy skies also varies significantly between these regions. In Japan, the MB indicates an average overestimation of +22.7 W·m^{-2}, with a wide range spanning from −80.9 to +125.2 W·m^{-2}. Conversely, the African sites display a diverse pattern of estimation errors; GOB records a median MB of −77.3 W·m^{-2}, suggesting a predominant underestimation, whereas VUW shows an overestimation, with a median MB of +20.6 W·m^{-2}. The KSA location experiences a minimal underestimation with a median MB of −15.6 W·m^{-2}, ranging narrowly from −30.9 to −2.2 W·m^{-2}, as depicted in Figure 5E. The satellite estimates particularly performed well in KSA and HON locations, as indicated by the lower IQRs and ranges of MB in these locations (Figure 5E).

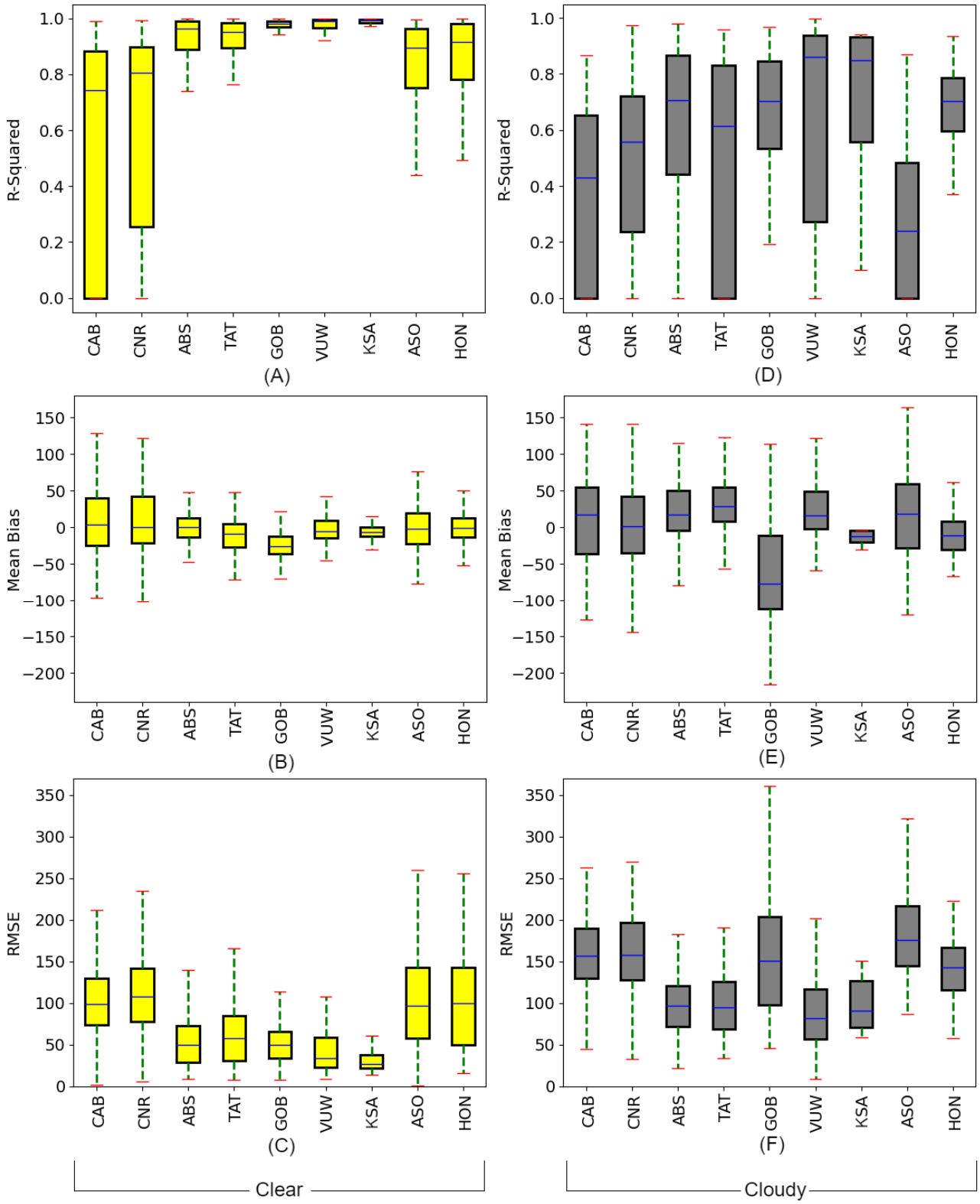


Figure 5. Comparison of ground and Heliosat-2 GHI estimates in terms of R^2, MB (in $W \cdot m^{-2}$), and RMSE (in $W \cdot m^{-2}$) values for the diurnal radiation, considering both clear (left column) and cloudy (right column) sky conditions. Clear-sky conditions (**A**–**C**) are characterized by high agreement indices (R^2) and low error indices (MB and RMSE), as compared to cloudy-sky conditions (**D**–**F**) for all the sites.

Additionally, the RMSE increases across all locations during cloudy conditions, indicating greater variability in solar radiation estimates. Japan experiences a substantial spread in RMSE values, from 23.7 to 185.9 W·m^{-2}, with a median of approximately 95.8 W·m^{-2}. As for the African sites, GOB in particular shows higher RMSE values, of 151.3 compared to VUW's 84.9 W·m^{-2}, suggesting a higher error magnitude under cloudy skies at the GOB site (Figure 5F). The KSA location also sees an elevation in RMSE, with values ranging from 62.3 to 148.2 W·m^{-2} and a median of about 91.8 W·m^{-2}, reinforcing the global trend of increased uncertainty in solar radiation measurements during cloudier weather. The locations of EU, GOB, and ASO show higher RMSE values, consistently reaching up to 150.0 W·m^{-2}, under cloudy days (Figure 5F).

3.3. Validation of Diurnal Solar Radiation in Different Months

When evaluating GHI estimates from Heliosat-2 on a monthly basis, using a dataset which includes both clear and cloudy days, the R^2 values in the EU locations were consistently lower than any other location in the study (<0.65). The months of January, February, and November, in these locations, demonstrated very low R^2 values, going below 0.3. In contrast, R^2 values in the ABS and TAT locations of Japan remained impressively robust, consistently topping 0.75 (Figure 6A). Notably, in March, May, and June, these values often exceeded 0.85. In African locations, R^2 values remain exceptionally high throughout the year, particularly from July through November, frequently surpassing 0.92. Similarly, in the KSA location, R^2 values are consistently high, generally exceeding 0.93, with peaks often reaching above 0.97 during January, August, and September (Figure 6A). In Indian sites, during the monsoon months, the R^2 values were lower (<0.7) compared to the non-monsoon months (>0.7).

EU sites, such as CAB and CNR, consistently display positive mean biases, indicating an overestimation of solar irradiance throughout the year, with CAB values ranging from 15.91 to 37.96 W·m^{-2} and CNR from 8.91 to 38.58 W·m^{-2}. On the monthly scale, MB values at Japanese sites fluctuate between −30.6 and +40.7 W·m^{-2}, with notable instances of overestimation, and often exceeding +30.0 W·m^{-2}, particularly between March and April and August-September (Figure 6B). In contrast, at the African sites, GOB consistently shows a trend of underestimation, with values ranging from −11.1 to −50.0 W·m^{-2}, while VUW exhibits a general overestimation, with values ranging from 0 to +38.1 W·m^{-2}. The KSA location in Saudi Arabia sees MB values ranging from −13.5 to +12.2 W·m^{-2}, with very slight underestimations typically observed during January, September, and November; these range from −5.9 to +2.2 W·m^{-2} (Figure 6B). In India, the performance of solar irradiance estimation using the Heliosate-2 method demonstrates a mixed pattern across the year. MB values for Indian sites, such as ASO and HON, vary notably, with ASO experiencing a range from −16.26 to 8.0 W·m^{-2} and HON from −17.8 to 15.8 W·m^{-2}, indicating both overestimation and underestimation of solar irradiance.

In a monthly study, the RMSE values for EU sites are notably higher, with CAB and CNR recording values ranging from 72.0 to 166.0 W·m^{-2} and 78.1 to 179.6 W·m^{-2}, respectively (Figure 6C). In the Japanese sites, notably lower RMSE values are observed between January and March and October-December, typically falling below 65.0 W·m^{-2}. African sites show a pattern of lower RMSE during the cooler months of July, August, and September (below 60.0 W·m^{-2}), whereas the warmer months of January, February, March, and December exhibit higher RMSE values, ranging from 95.0 to 130.0 W·m^{-2}, as illustrated in Figure 6C. At the KSA site in Saudi Arabia, RMSE values are exceptionally low, mostly below 50.2 W·m^{-2}, with January and September marking months where RMSE values are consistently below 30.0 W·m^{-2}. In India, the RMSE values remain relatively lower, with ASO and HON registering values ranging from 35.4 to 215.5 W·m^{-2} and 60.1 to 146.8 W·m^{-2}, respectively.

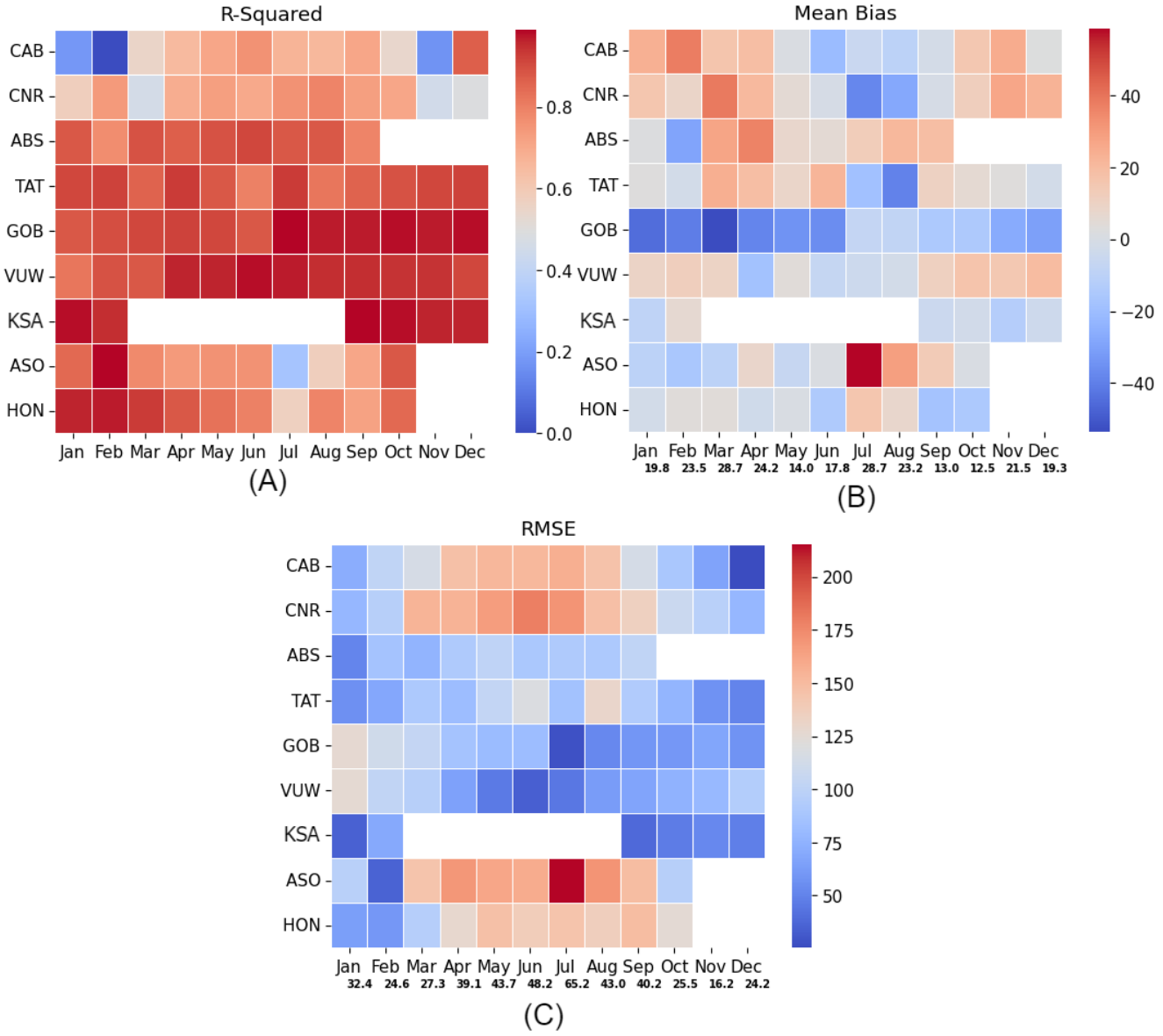


Figure 6. Comparison of ground-based and Heliosat-2 GHI estimates in terms of (**A**) R^2, (**B**) MB (in $W \cdot m^{-2}$), and (**C**) RMSE (in $W \cdot m^{-2}$) values for diurnal radiation across different months. The blank spaces indicate null values occurring due to the unavailability of ground data. Noticeably, the monsoon months (June-September) in Indian sites (ASO and HON), as well as in EU sites, exhibit higher error values. These months are also characterized by high levels of standard error, as shown below the month labels in the MB and RMSE heatmaps. In contrast, KSA in Saudi Arabia is characterized by high R^2 and low RMSE values.

4. Discussion

Ensuring the comparability of data from the MSG and Himawari-8 satellites is crucial for the integrity of our study. We took several steps to ensure that the data was consistent and reliable. We used images from both satellites, focusing on similar channels near the 0.6 µm spectral band, and re-gridded the images to a common resolution of 3 km to reduce errors. We also applied the Heliosat-2 method, which uses a standardized cloudiness index, to keep our cloud-cover assessments consistent. Despite our efforts, we recognize that some differences might still exist. To address this, we presented our findings using box plots across different quantiles, giving a more comprehensive view of the data and minimizing the impact of any remaining discrepancies.

A blended method of estimation of all-sky GHI Heliosat-2 is proposed in this study, one adopted from Bechet et al. [27] and Cros et al. [41], who contributed significantly to the field of solar irradiance modeling, though they focused on different aspects. Bechet et al.'s H2-hybrid model emphasizes the importance of cloud cover in its effect on solar irradiance, using a cloudiness index to estimate GHI. On the other hand, Cros et al.'s work enhances this approach by incorporating a wider range of atmospheric data, including aerosols, ozone, and water vapor, through radiative transfer modeling, enabling increasingly precise calculations of spectrally resolved all-sky radiance. These methods complement each other by focusing on both specific and comprehensive atmospheric factors that influence solar irradiance, suggesting the potential of integrated approaches in more accurately modeling and utilizing solar energy data. Notably, cloud cover and aerosols play significant roles in the absorption and diffusion of solar radiation, which further emphasizes the importance of distinguishing between clear-sky and cloudy-sky conditions when evaluating surface solar radiation and air pollution dynamics [47]. Hence, we move into the following discussion to explore how these integrated approaches perform under varying weather conditions, particularly focusing on estimation biases during cloudy and clear days.

4.1. Estimation Bias Based on Weather: Cloudy vs. Clear

In our study, we observed that during cloudy days, the estimates provided by Heliosat-2 generally exceeded the ground measurements data in both Japanese locations and one African location. Conversely, on clear days, there was a tendency for underestimation, as indicated by the median value of the MB across all study locations. The proportion of cloudy days sampled (ranging from 19.9% to 41.23% across all regions in our study) was notably lower compared to the total sample of clear days (ranging from 58.77% to 81.1%), as demonstrated in Table 2. This result can be linked to the finding of [48], which employed FY-4A satellite images to derive GHI using the Heliosat-2 methodology across four locations in China, from June 2018 to May 2019. Their findings mirrored ours, indicating a tendency to overestimate GHI in locations with limited ground-observed data and to underestimate it when such data were more abundant.

Table 2. Representation of the numbers of clear and cloudy days across all the locations in the current investigation. Here, N_{Clouds} represents the number of cloudy days and N_{Clear} represents the number of clear-sky days. The % estimates of the number of cloudy and clear days are given in the last two columns.

Site	N_{Cloudy}	N_{Clear}	Total Days	% N_{Cloudy}	% N_{Clear}
CAB	167	596	763	21.89	78.12
CNR	136	624	760	17.89	82.11
ABS	132	140	272	48.53	51.47
TAT	143	252	395	36.20	63.80
GOB	88	642	730	12.05	87.95
VUW	240	490	730	32.88	67.12
KSA	55	150	205	26.83	73.17
ASO	74	229	303	24.42	75.58
HON	82	220	302	27.15	72.85
Regional Analysis (Sum)					
Locations in Europe	303	1220	1523	19.9	81.1
Locations in East Asia	275	392	667	41.23	58.77
Location in Africa	328	1132	1460	22.47	77.53
Location in the Middle East	55	150	205	26.83	73.17
Locations in South Asia	156	449	605	25.8	74.2

Studies [49–52], focusing on different versions of Heliosat, similarly noted a general underestimation of GHI values by the model during cloudy-sky conditions. GHI estimation from SENSE2 (Solar Energy Nowcasting System) [53] also observed an overestimation of

GHI under cloudy-sky conditions. They attributed this to the uncertainties associated with cloud-related information within the satellite pixel. Additionally, they noted a relatively low underestimation linked with aerosol optical depth (AOD). In line with our findings, these studies underscore the influences of sky conditions and satellite data uncertainties on GHI estimation accuracy.

In the context of solar energy estimation, clear-sky models provide estimates assuming cloudless conditions, considering factors like solar elevation angle, site altitude, and atmospheric properties. However, these models often underestimate the impact of cloud cover. Cloudy-sky conditions, on the other hand, account for cloud scattering and absorption of sunlight, leading to overestimation due to clear-sky assumptions. Real-world observations consider dynamic effects, resulting in differences between estimated and measured GHI, while clear-sky models serve as useful benchmarks, understanding the complexities of cloud influence is crucial for accurate solar resource assessments

In the current investigation, the performance of Heliosat-2 was primarily analyzed based on cloudy and clear days and using the clearness index. Cloud cover and aerosols significantly influence the absorption and diffusion of solar radiation, emphasizing the importance of differentiating between clear-sky and cloudy-sky conditions when evaluating surface solar radiation and air-pollution dynamics [47]. Notably, clear days with significant pollutants can behave similarly to cloudy days due to the scattering effect of solar radiation caused by atmospheric pollutants. For instance, [47] reported that clear days with substantial particulate matter of size 2.5 μm (PM2.5) or less result in more solar radiation scattering at the surface, compared to days when there are significant PM10 in the atmosphere. Absorbing aerosols decrease both direct normal irradiance (DNI) and diffuse horizontal irradiance (DHI), while non-absorbing aerosols decrease DNI but increase DHI.

4.2. Comparison of GHI Studies

A study reported in [54] reported an RMSE of 73.8 $W{\cdot}m^{-2}$ and an MB of -3.7 $W{\cdot}m^{-2}$, indicating commendable accuracy but one with a slight bias towards underestimation. Conversely, [54] exhibited a higher RMSE, of 85.3 $W{\cdot}m^{-2}$, and a significant bias (MB = 20.8 $W{\cdot}m^{-2}$), yet maintained a strong correlation with ground measurements (R^2 = 0.91). Our study surpassed both predecessors, boasting an RMSE of 65.0 $W{\cdot}m^{-2}$, a minimal bias (MB = -5.1 $W{\cdot}m^{-2}$), and a similar R^2 value of 0.94. These results signify advancements in GHI estimation techniques, highlighting the efficacy of our methodological approach in achieving heightened precision and reliability.

In the TAT location, located in Japan, over the period from 2010 to 2014, the variability in MB highlights the different challenges described in the study of [55]. ERA5 shows a negative MB of -1.2 $kW{\cdot}m^{-2}$, which may indicate underestimation of actual solar radiation levels. Both ERA-Interim and MERRA2 report positive biases (11.9 $kW{\cdot}m^{-2}$ and 19.1 $kW{\cdot}m^{-2}$, respectively), suggesting that these models tend to overestimate solar radiation in this location. Our study indicates an MB of -5.1 $kW{\cdot}m^{-2}$, further reinforcing the trend of underestimation observed in some datasets.

4.3. Regional and Seasonal Variability in Solar Irradiance

The analyses of high RMSE and MB, as well as low R^2 values, in certain months across different locations reveals significant insights into the regional and temporal variability of solar irradiance estimation using Heliosat-2. In Europe, locations like CAB and CNR experience high RMSE values, particularly during winter months (e.g., January, February, and November), which coincides with low R^2 values, which drop below 0.3. The substantial seasonal variability, including cloudy weather and low solar angles, contributes to these discrepancies. The persistently positive MB values in CAB and CNR indicate a tendency to overestimate solar irradiance due to frequent cloud cover and varying atmospheric conditions such as aerosols and humidity levels [56].

Japanese sites, such as ABS and TAT, demonstrate consistently high R^2 values, often exceeding 0.85 in March, May, and June, and robust values throughout the year. This

stability is due to relatively predictable weather patterns and moderate latitudes [57,58]. However, the MB values fluctuate, with significant overestimation during March-April and August-September, reflecting seasonal changes and specific events like the cherry blossom season. The RMSE values are notably lower, usually falling below 65.0 $W \cdot m^{-2}$ between January and March and October-December.

In African regions, such as GOB and VUW, the R^2 values remain exceptionally high throughout the year, particularly from July to November, frequently surpassing 0.92. The RMSE values, however, are higher during warmer months (January, February, March, and December) and lower during cooler months (July, August, and September). GOB consistently shows a trend of underestimation, which is attributed to reflective desert surfaces. VUW exhibits a general overestimation, one influenced by seasonal vegetative changes affecting ground albedo [59,60].

In Saudi Arabia, the R^2 values are consistently high, generally exceeding 0.93, with peaks often rising above 0.97 during January, August, and September. The MB values indicate that the GHI estimates of the model are generally underestimated during January, September, and November. The RMSE values are exceptionally low, mostly below 50.2 $W \cdot m^{-2}$, with January and September showing values consistently below 30.0 $W \cdot m^{-2}$, due to the clear desert skies and minimal atmospheric disturbances [61].

In India, sites like ASO and HON show a distinct seasonal pattern, with lower R^2 values during monsoon months (June-September) due to heavy cloud cover and unpredictable weather. The monsoon season significantly impacts solar irradiance estimation by introducing dense cloud formations, high humidity, and frequent rainfall, all of which reduce the accuracy of the model [62]. The MB values for ASO and HON indicate both overestimation and underestimation, influenced by seasonal variability. The RMSE values are relatively lower, reflecting the impacts of monsoon and non-monsoon periods.

The deviations in R^2, MB, and RMSE values across different locations and months are driven by climatic and geographical factors such as weather variability, solar angles, atmospheric conditions, and surface reflectivity. In particular, the monsoon season in India, with its heavy cloud cover and frequent rain, greatly affects the accuracy of solar irradiance estimates, highlighting the influences of local weather processes on solar energy modeling. These factors collectively influence the accuracy of solar irradiance estimates, leading to significant monthly and regional deviations.

5. Conclusions

In conclusion, the comparative analysis considering the Heliosat-2 solar radiation estimates and ground measurements from diverse sources like BSRN, SAURAN, and SCADA, ranging across various geographic regions, provides significant insights into the model's accuracy and reliability.

In the realm of solar energy estimation, clear-sky models offer projections under the assumption of cloudless atmospheres, factoring in variables such as solar elevation angle, site altitude, and atmospheric characteristics. Nonetheless, these models often fall short in accurately assessing the influence of cloud cover. Conversely, cloudy-sky conditions consider the scattering and absorption of sunlight by clouds, resulting in an overestimation attributable to the assumptions of clear-sky scenarios. The study reveals a tendency for Heliosat-2 Global Horizontal Irradiance (GHI) estimates to overestimate during cloudy conditions and underestimate on clear days. This phenomenon can also be attributed to the lower sample size for the cloudy days, compared to that for clear days.

The performance of Heliosat-2 in various locations demonstrates its efficacy in solar energy planning and radiation estimation. In Japan, despite notable variability in RMSE during cloudy days, the model achieves high median R^2 values on clear days, indicating robust performance. Similarly, in South Africa and Namibia, Heliosat-2 exhibits commendable accuracy, with a majority of data points falling within acceptable ranges. Although slight underestimations are observed in Saudi Arabia, particularly on cloudy

days, the model consistently achieves high R^2 values, affirming its reliability as to solar radiation estimation.

In general, the study confirms the effectiveness of Heliosat-2 in providing reliable solar radiation estimates across diverse geographic regions and varying weather conditions. While slight deviations are noted under cloudy conditions, the model's ability to maintain high accuracy during clear skies highlights its potential for widespread application in solar energy resource assessment and planning. Future research should focus on analyzing the performance of Heliosat-2 under varying pollution levels, including different types and sizes of aerosol particles.

Author Contributions: Conceptualization, S.H.A.R. and R.C.; Data curation, J.K.M. and R.K.; Formal analysis, J.K.M.; Investigation, J.K.M.; Methodology, J.K.M.; Project administration, S.H.A.R., B.C., and R.C.; Resources, R.K.; Software, B.C. and Y.T.; Supervision, J.K.M. and S.H.A.R.; Validation, J.K.M.; Visualization, J.K.M.; Writing—original draft, J.K.M.; Writing—review and editing, S.H.A.R. and V.S. All authors have read and agreed to the published version of the manuscript.

Funding: This research was fully funded by Solarad AI Private Limited. Solarad AI provided financial support and resources for the conduct of this research. The analysis and interpretation of data, as well as the decision to publish these findings, were carried out independently by the authors, ensuring the scientific rigor and integrity of the research.

Data Availability Statement: The BSRN datasets are publicly accessible via https://bsrn.awi.de/. SAURAN data can be retrieved from the public repository at https://sauran.ac.za/. Himawari-8 images, intended solely for research and educational purposes, are freely obtainable from https://himawari8.nict.go.jp/ following registration with the HIMAWARI administration. Similarly, images from MSG can be acquired from https://view.meteosat.int/. Heliosat-2 estimate datasets will be provided upon request. However, due to a Non-Disclosure Agreement (NDA) with the respective clients, access to SCADA data is contingent upon signing an NDA with the requesting agency.

Acknowledgments: The authors would like to express their sincere gratitude to the anonymous reviewers for their constructive comments and valuable suggestions, which have significantly improved the quality and clarity of this manuscript. Their dedication and expertise have been instrumental in refining our work, and we are deeply appreciative of the time and effort they invested in the review process. All the authors wish to express their gratitude to the administrators of BSRN, SAURAN, JMA, and EUMETSAT for generously providing access to their datasets, without which this research could not have been accomplished successfully. Additionally, the funding support extended by Solarad AI Private Limited is gratefully acknowledged.

Conflicts of Interest: Authors Jitendra Kumar Meher, Syed Haider Abbas Rizvi, Bhramar Choudhary, Ravi Choudhary, Yash Thakre and Ritesh Kumar were employed by the company Solarad AI. The remaining authors declare that the research was conducted in the absence of any commercial or financial relationships that could be construed as a potential conflict of interest. The authors declare that this study received funding from Solarad AI. The funder was not involved in the study design, collection, analysis, interpretation of data, the writing of this article or the decision to submit it for publication.

References

1. Habte, A.; Sengupta, M.; Lopez, A. *Evaluation of the National Solar Radiation Database (NSRDB): 1998–2015*; No. NREL/TP-5D00-67722; National Renewable Energy Lab (NREL): Golden, CO, USA, 2017. Available online: https://www.nrel.gov/docs/fy17osti/67722.pdf (accessed on 10 April 2024).
2. Zhang, J.; Zhao, L.; Deng, S.; Xu, W.; Zhang, Y. A Critical Review of the Models Used to Estimate Solar Radiation. *Renew. Sustain. Energy Rev.* **2017**, *70*, 314–329. [CrossRef]
3. Sen, Z. *Solar Energy Fundamentals and Modeling Techniques: Atmosphere, Environment, Climate Change, and Renewable Energy*; Springer Science & Business Media: London, UK, 2008. [CrossRef]
4. Sengupta, M.; Habte, A.; Wilbert, S.; Gueymard, C.; Remund, J. *Best Practices Handbook for the Collection and Use of Solar Resource Data for Solar Energy Applications*; No. NREL/TP-5D00-77635; National Renewable Energy Lab (NREL): Golden, CO, USA, 2021.
5. Driemel, A.; Augustine, J.; Behrens, K.; Colle, S.; Cox, C.; Cuevas-Agulló, E.; Denn, F.M.; Duprat, T.; Fukuda, M.; Grobe, H.; et al. Baseline Surface Radiation Network (BSRN): Structure and Data Description (1992–2017). *Earth Syst. Sci. Data* **2018**, *10*, 1491–1501. [CrossRef]

6. Hatzianastassiou, N.; Ioannidis, E.; Korras-Carraca, M.B.; Gavrouzou, M.; Papadimas, C.D.; Matsoukas, C.; Benas, N.; Fotiadi, A.; Wild, M.; Vardavas, I. Global Dimming and Brightening Features during the First Decade of the 21st Century. *Atmosphere* **2020**, *11*, 308. [CrossRef]
7. Stamatis, M.; Hatzianastassiou, N.; Korras-Carraca, M.B.; Matsoukas, C.; Wild, M.; Vardavas, I. Interdecadal Changes of the MERRA-2 Incoming Surface Solar Radiation (SSR) and Evaluation against GEBA & BSRN Stations. *Appl. Sci.* **2022**, *12*, 10176. [CrossRef]
8. Schreck, S.; Schroedter-Homscheidt, M.; Klein, M.; Cao, K.K. Satellite Image-Based Generation of High Frequency Solar Radiation Time Series for the Assessment of Solar Energy Systems. *Meteorol. Z.* **2020**, *29*, 377–392. [CrossRef]
9. Balsamo, G.; Agusti-Parareda, A.; Albergel, C.; Arduini, G.; Beljaars, A.; Bidlot, J.; Blyth, E.; Bousserez, N.; Boussetta, S.; Brown, A.; et al. Satellite and In Situ Observations for Advancing Global Earth Surface Modelling: A Review. *Remote Sens.* **2018**, *10*, 2038. [CrossRef]
10. Valipour, M.; Dietrich, J. Developing Ensemble Mean Models of Satellite Remote Sensing, Climate Reanalysis, and Land Surface Models. *Theor. Appl. Climatol.* **2022**, *150*, 909–926. [CrossRef]
11. Prasad, A.A.; Kay, M. Prediction of Solar Power Using Near-Real Time Satellite Data. *Energies* **2021**, *14*, 5865. [CrossRef]
12. Baatz, R.; Hendricks Franssen, H.J.; Euskirchen, E.; Sihi, D.; Dietze, M.; Ciavatta, S.; Fennel, K.; Beck, H.; De Lannoy, G.; Pauwels, V.R.N.; et al. Reanalysis in Earth System Science: Toward Terrestrial Ecosystem Reanalysis. *Rev. Geophys.* **2021**, *59*, e2020RG000715. [CrossRef]
13. Huang, G.; Li, Z.; Li, X.; Liang, S.; Yang, K.; Wang, D.; Zhang, Y. Estimating Surface Solar Irradiance from Satellites: Past, Present, and Future Perspectives. *Remote Sens. Environ.* **2019**, *233*, 111371. [CrossRef]
14. Cano, D.; Monget, J.M.; Albuisson, M.; Guillard, H.; Regas, N.; Wald, L. A Method for the Determination of the Global Solar Radiation from Meteorological Satellite Data. *Sol. Energy* **1986**, *37*, 31–39. [CrossRef]
15. Rigollier, C.; Lefèvre, M.; Wald, L. The Method Heliosat-2 for Deriving Shortwave Solar Radiation from Satellite Images. *Sol. Energy* **2004**, *77*, 159–169. [CrossRef]
16. Yang, L.; Gao, X.; Hua, J.; Wu, P.; Li, Z.; Jia, D. Very Short-Term Surface Solar Irradiance Forecasting Based on FengYun-4 Geostationary Satellite. *Sensors* **2020**, *20*, 2606. [CrossRef] [PubMed]
17. Thaker, J.; Höller, R.; Kapasi, M. Short-Term Solar Irradiance Prediction with a Hybrid Ensemble Model Using METEOSAT Satellite Images. *Energies* **2024**, *17*, 329. [CrossRef]
18. El Alani, O.; Ghennioui, H.; Abraim, M.; Ghennioui, A.; Blanc, P.; Saint-Drenan, Y.M.; Naimi, Z. Solar Energy Resource Assessment Using GHI and DNI Satellite Data for Moroccan Climate. In *International Conference on Advanced Technologies for Humanity*; Springer International Publishing: Cham, Switzerland, 2022; pp. 275–285. [CrossRef] [PubMed]
19. Verma, P.; Patil, S. A Machine Learning Approach and Methodology for Solar Radiation Assessment Using Multispectral Satellite Images. *Ann. Data Sci.* **2023**, *10*, 907–932. [CrossRef]
20. Huang, C.; Shi, H.; Yang, D.; Gao, L.; Zhang, P.; Fu, D.; Chen, Q.; Yuan, Y.; Liu, M.; Hu, B.; et al. Retrieval of Sub-Kilometer Resolution Solar Irradiance from Fengyun-4A Satellite Using a Region-Adapted Heliosat-2 Method. *Sol. Energy* **2023**, *264*, 112038. [CrossRef]
21. Vuilleumier, L.; Meyer, A.; Stöckli, R.; Wilbert, S.; Zarzalejo, L.F. Accuracy of satellite-derived solar direct irradiance in Southern Spain and Switzerland. *Int. J. Remote Sens.* **2020**, *41*, 8808–8838. [CrossRef]
22. Polo, J.; Zarzalejo, L.F.; Cony, M.; Navarro, A.A.; Marchante, R.; Martin, L.; Romero, M. Solar Radiation Estimations over India Using Meteosat Satellite Images. *Sol. Energy* **2011**, *85*, 2395–2406. [CrossRef]
23. Masoom, A.; Kosmopoulos, P.; Bansal, A.; Kazadzis, S. Solar Energy Estimations in India Using Remote Sensing Technologies and Validation with Sun Photometers in Urban Areas. *Remote Sens.* **2020**, *12*, 254. [CrossRef]
24. Ameen, B.; Balzter, H.; Jarvis, C.; Wey, E.; Thomas, C.; Marchand, M. Validation of Hourly Global Horizontal Irradiance for Two Satellite-Derived Datasets in Northeast Iraq. *Remote Sens.* **2018**, *10*, 1651. [CrossRef]
25. Sarr, A.; Kebe, C.M.F.; Ndiaye, A. Validation of Helioclim-3 irradiance with ground observations in Senegal using four typical climatic zones. *Mater. Today Proc.* **2022**, *51*, 1888–1895. [CrossRef]
26. Syu, M.R.; Lee, P.H.; Leou, T.M.; Shen, Y. Solar Irradiance and Pan Evaporation Estimation from Meteorological Satellite Data. *Terr. Atmos. Ocean. Sci.* **2016**, *27*, 221–239. [CrossRef] [PubMed]
27. Bechet, J.; Albarelo, T.; Macaire, J.; Salloum, M.; Zermani, S.; Primerose, A.; Linguet, L. Updated GOES-13 Heliosat-2 Method for Global Horizontal Irradiation in the Americas. *Remote Sens.* **2022**, *14*, 224. [CrossRef]
28. Brooks, M.J.; Du Clou, S.; Van Niekerk, W.L.; Gauché, P.; Leonard, C.; Mouzouris, M.J.; Meyer, R.; Van der Westhuizen, N.; Van Dyk, E.E.; Vorster, F.J. SAURAN: A New Resource for Solar Radiometric Data in Southern Africa. *J. Energy South. Afr.* **2015**, *26*, 2–10. [CrossRef]
29. Knap, W. *Basic and Other Measurements of Radiation at Station Cabauw (2005-02 et seq) [Dataset Publication Series]*; Koninklijk Nederlands Meteorologisch Instituut: De Bilt, The Netherlands, 2022. [CrossRef]
30. Olano, X. *Basic Measurements of Radiation at Station Cener (2009-07 et seq) [Dataset Publication Series]*; National Renewable Energy Centre: Navarra, Spain, 2021. [CrossRef]
31. Ohtake, J. *Basic Measurements of Radiation at Station Abashiri (2021-04) [Dataset]*; Japan Meteorological Agency: Tokyo, Japan, 2021. [CrossRef]

32. Ijima, O. *Basic and Other Measurements of Radiation at Station Tateno (2020-12) [Dataset]*; Aerological Observatory, Japan Meteorological Agency: Tokyo, Japan, 2021. [CrossRef]
33. Vogt, R. Basic and Other Measurements of Radiation at Station Gobabeb (2013-09). [Online]. 2013. Available online: https://doi.pangaea.de/10.1594/PANGAEA.821500 (accessed on 12 April 2024).
34. Long, C.N.; Shi, Y. The QCRad value added product: Surface radiation measurement quality control testing, including climatology configurable limits. In *Atmospheric Radiation Measurement Program Technical Report*; DOE Office of Science Atmospheric Radiation Measurement (ARM) Program: Washington, DC, USA, 2006. [CrossRef]
35. Ouiqary, A.E.; Kheddioui, E.; Smiej, M.F. Evaluation of the Global Horizontal Irradiation (GHI) on the Ground from the Images of the Second Generation European Meteorological Satellites MSG. *J. Comput. Commun.* **2023**, *11*, 1–11. [CrossRef]
36. Guo, H.; Chen, S.; Bao, A.; Hu, J.; Gebregiorgis, A.S.; Xue, X.; Zhang, X. Inter-comparison of high-resolution satellite precipitation products over Central Asia. *Remote Sens.* **2015**, *7*, 7181–7211. [CrossRef]
37. Meher, J.K.; Das, L.; Akhter, J.; Benestad, R.E.; Mezghani, A. Performance of CMIP3 and CMIP5 GCMs to simulate observed rainfall characteristics over the Western Himalayan region. *J. Clim.* **2017**, *30*, 7777–7799. [CrossRef]
38. Chen, A.; Chen, D.; Azorin-Molina, C. Assessing reliability of precipitation data over the Mekong River Basin: A comparison of ground-based, satellite, and reanalysis datasets. *Int. J. Climatol.* **2018**, *38*, 4314–4334. [CrossRef]
39. Bird, R.E.; Hulstrom, R.L. *Simplified Clear Sky Model for Direct and Diffuse Insolation on Horizontal Surfaces*; Solar Energy Research Institute (SERI): Golden, CO, USA, 1981; No. SERI/TR-642-761.
40. Annear, R.L.; Wells, S.A. A comparison of five models for estimating clear-sky solar radiation. *Water Resour. Res.* **2007**, *43*, W10415, 1–15. [CrossRef]
41. Cros, S.; Badosa, J.; Szantaï, A.; Haeffelin, M. Reliability predictors for solar irradiance satellite-based forecast. *Energies* **2020**, *13*, 5566. [CrossRef]
42. Marie-Joseph, I.; Linguet, L.; Gobinddass, M.L.; Wald, L. On the applicability of the Heliosat-2 method to assess surface solar irradiation in the Intertropical Convergence Zone, French Guiana. *Int. J. Remote Sens.* **2013**, *34*, 3012–3027. [CrossRef]
43. Boilley, A.; Wald, L. Comparison between meteorological reanalyses from ERA-Interim and MERRA and measurements of daily solar irradiation at surface. *Renew. Energy* **2015**, *75*, 135–143. [CrossRef]
44. Correa, L.F.; Folini, D.; Chtirkova, B.; Wild, M. A method for clear-sky identification and long-term trends assessment using daily surface solar radiation records. *Earth Space Sci.* **2022**, *9*, e2021EA002197. [CrossRef]
45. Holmgren, W.F.; Hansen, C.W.; Mikofski, M.A. pvlib python: A python package for modeling solar energy systems. *J. Open Source Softw.* **2018**, *3*, 884. [CrossRef]
46. Holmgren, W.F.; Anderson, K.; Hansen, C.; Robwandrews; Mikofski, M.; Jensen, A.R. *pvlib/pvlib-python: v0.10.4*; Zenodo: Geneva, Switzerland, 2024.
47. Luo, H.; Han, Y.; Lu, C.; Yang, J.; Wu, Y. Characteristics of surface solar radiation under different air pollution conditions over Nanjing, China: Observation and simulation. *Adv. Atmos. Sci.* **2019**, *36*, 1047–1059. [CrossRef]
48. Jia, D.; Hua, J.; Wang, L.; Guo, Y.; Guo, H.; Wu, P.; Liu, M.; Yang, L. Estimations of global horizontal irradiance and direct normal irradiance by using Fengyun-4A satellite data in northern China. *Remote Sens.* **2021**, *13*, 790. [CrossRef]
49. Oumbe, A.; Blanc, P.; Ranchin, T.; Homscheidt, M.S.; Wald, L. A new method for estimating solar energy resource. In Proceedings of the 33rd International Symposium on Remote Sensing of Environment (ISRSE 33), Stresa, Italy, 4–9 May 2009; Joint Research Center: HAL Open Science: Paris, France, 2009. paper-773. Available online: https://core.ac.uk/download/pdf/51233394.pdf (accessed on 11 May 2024).
50. Qu, Z.; Oumbe, A.; Blanc, P.; Espinar, B.; Gesell, G.; Gschwind, B.; Klüser, L.; Lefèvre, M.; Saboret, L.; Schroedter-Homscheidt, M.; et al. Fast radiative transfer parameterisation for assessing the surface solar irradiance: The Heliosat-4 method. *Meteorol. Z.* **2017**, *26*, 33–57. [CrossRef]
51. Mouhamet, D.; Tommy, A.; Primerose, A.; Laurent, L. Improving the Heliosat-2 method for surface solar irradiation estimation under cloudy sky areas. *Sol. Energy* **2018**, *169*, 565–576. [CrossRef]
52. Papachristopoulou, K.; Fountoulakis, I.; Bais, A.F.; Psiloglou, B.E.; Papadimitriou, N.; Raptis, I.P.; Kazantzidis, A.; Kontoes, C.; Hatzaki, M.; Kazadzis, S. Effects of clouds and aerosols on downwelling surface solar irradiance nowcasting and short-term forecasting. *Atmos. Meas. Tech.* **2024**, *17*, 1851–1877. [CrossRef]
53. Li, J.; Tang, W.; Qi, J.; Yan, Z. Mapping high-resolution surface shortwave radiation over East Asia with the new generation geostationary meteorological satellite Himawari-8. *Int. J. Digit. Earth* **2023**, *16*, 323–336. [CrossRef]
54. Yu, Y.; Shi, J.; Wang, T.; Letu, H.; Yuan, P.; Zhou, W.; Hu, L. Evaluation of the Himawari-8 shortwave downward radiation (SWDR) product and its comparison with the CERES-SYN, MERRA-2, and ERA-interim datasets. *IEEE J. Sel. Top. Appl. Earth Obs. Remote Sens.* **2018**, *12*, 519–532. [CrossRef]
55. Urraca, R.; Huld, T.; Gracia-Amillo, A.; Martinez-de-Pison, F.J.; Kaspar, F.; Sanz-Garcia, A. Evaluation of global horizontal irradiance estimates from ERA5 and COSMO-REA6 reanalyses using ground and satellite-based data. *Sol. Energy* **2018**, *164*, 339–354. [CrossRef]
56. Ruosteenoja, K.; Räisänen, P. Seasonal changes in solar radiation and relative humidity in Europe in response to global warming. *J. Clim.* **2013**, *26*, 2467–2481. [CrossRef]
57. Sevillano-Bendezú, M.A.; Khenkin, M.; Nofuentes, G.; De la Casa, J.; Ulbrich, C.; Töfflinger, J.A. Predictability and interrelations of spectral indicators for PV performance in multiple latitudes and climates. *Sol. Energy* **2023**, *259*, 174–187. [CrossRef]

58. Baba, Y. Improvements in SINTEX-F2 seasonal prediction by implementing an atmospheric nudging scheme. *Int. J. Climatol.* **2023**, *43*, 6900–6923. [CrossRef]
59. Smoliak, B.V.; Gelobter, M.; Haley, J.T. Mapping potential surface contributions to reflected solar radiation. *Environ. Res. Commun.* **2022**, *4*, 065003. [CrossRef]
60. Roccetti, G.; Bugliaro, L.; Gödde, F.; Emde, C.; Hamann, U.; Manev, M.; Sterzik, M.F.; Wehrum, C. Development of a HAMSTER: Hyperspectral Albedo Maps dataset with high Spatial and TEmporal Resolution. *EGUsphere* **2024**, 1–27. [CrossRef]
61. Farahat, A.; Kambezidis, H.D.; Labban, A. The Solar Radiation Climate of Saudi Arabia. *Climate* **2023**, *11*, 75. [CrossRef]
62. Li, Z.; Lau, W.M.; Ramanathan, V.; Wu, G.; Ding, Y.; Manoj, M.G.; Liu, J.; Qian, Y.; Li, J.; Zhou, T.; et al. Aerosol and monsoon climate interactions over Asia. *Rev. Geophys.* **2016**, *54*, 866–929. [CrossRef]

Disclaimer/Publisher's Note: The statements, opinions and data contained in all publications are solely those of the individual author(s) and contributor(s) and not of MDPI and/or the editor(s). MDPI and/or the editor(s) disclaim responsibility for any injury to people or property resulting from any ideas, methods, instructions or products referred to in the content.